Selective Anion Manipulation for Controlling Thermoelectric Properties of Epitaxial SnO_2 Films on r-Al_2O_3

*Takafumi Ishibe[1], Seiya Kozuki[1], Yuki Komatsubara[1], Yuto Uematsu[1], Takashi Yoshizaki[1], Yuichiro Yamashita[2], Nobuyasu Naruse[3], Yutaka Mera[3], Eiichi Kobayashi[4], and Yoshiaki Nakamura[1] **

1 Graduate School of Engineering Science, Osaka University, 1-3 Machikaneyama-cho, Toyonaka, Osaka 560-8531, Japan

2 National Institute of Advanced Industrial Science and Technology, 1-1-1 Umezono, Tsukuba, Ibaraki 305-8563, Japan

3 Department of Fundamental Bioscience, Shiga University of Medical Science, Otsu, Shiga 520-2192, Japan

4 Kyushu Synchrotron Light Research Center, 8-7 Yayoigaoka, Tosu, Saga 841-0005, Japan

*Corresponding author: nakamura.yoshiaki.es@osaka-u.ac.jp

(Previous address: nakamura@ee.es.osaka-u.ac.jp)

ABSTRACT

Introducing defects is one of the promising approaches for enhancing thermoelectric property. In this study, we substantially reduce thermal conductivity while maintaining a high thermoelectric power factor (PF) by selectively manipulating O^{2-} anion in domain-engineered SnO_2 with conduction and valence bands mainly composed of Sn5s and O2p orbitals, respectively. Ion implantation can generate O defects more easily than Sn defects, resulting in a small impact on Sn5s conduction band and the formation of O defect resonant level. The lattice thermal conductivity of the Arsenic-implanted epitaxial SnO_2 films with the manipulated O^{2-} anions (2.6 $Wm^{-1}K^{-1}$) is approximately half that of Sb-doped films without them (4.7 $Wm^{-1}K^{-1}$), while the maximum PF of Arsenic-implanted epitaxial SnO_2 films remains relatively high owing to the high Seebeck coefficient originating from an effective mass increase. This selective O^{2-} anion manipulation is an outstanding methodology of selectively causing thermal conductivity reduction while maintaining high PF.

KEYWORDS

Thermoelectric conversion, Anion, Phonon, Transparent oxide, Thin film, Epitaxy, SnO_2

INTRODUCTION

Thermoelectric (TE) conversion, which allows us the reuse of wasted heat as electrical energy, has drawn significant global attention in the world requiring energy-harvesting [1, 2] and energy-saving techniques [3]. TE conversion efficiency increases monotonically with dimensionless figure-of-merit zT ($=S^2\sigma T\kappa^{-1}$), where S is Seebeck coefficient, σ is electrical conductivity, κ is thermal conductivity, and T is absolute temperature. The interdependent relationship among the three TE parameters has prevented the acquisition of high zT [4-16]. Furthermore, in terms of social application compatibility, high-performance TE materials composed of low-cost and non-toxic elements are required.

Introducing defects is one of the promising approaches for zT enhancement [17-21]. Numerous studies have reported that the increase of defect phonon scattering drastically reduced κ [17-20]. However, $S^2\sigma$ usually becomes low due to defect carrier scattering. In recent years, some studies have reported that the resonant level formed by defect introduction enhanced the effective mass m^*, leading to high S [21, 22]. Defect selectivity is important for enhancing S while suppressing the decrease of mobility μ. For example, the defect resonant level must be so close to the conduction band minimum that it can hybridize with the conduction band [23]. In addition, the atoms composing the carrier conduction band should be undamaged [24, 25] to avoid μ deterioration which is unrelated to the resonant level effect.

In the case of oxide semiconductor crystals, which usually exhibit n-type behavior, the O^{2-} anion and metal cation orbitals mainly form valence and conduction bands, respectively. O defect is considered to likely make a small impact on electron conduction than the cation defect. On the other hand, if the O defect level is close to the conduction band minimum, the O defect resonant level can be formed, increasing m^*. Therefore, selectively manipulating the O^{2-} anion can increase S while suppressing a μ decrease. However, no studies on TE have achieved this for oxide TE crystals.

In 2021, with the aim toward the transparent TE power generation, we simultaneously realized high μ and relatively-low κ (5.1 $Wm^{-1}K^{-1}$) in transparent single-crystalline SnO_2 films with a thickness of

~120 nm composed of low-cost and non-toxic elements through domain engineering [26], that is, the introduction of nanoscale interface with low defect areal density by controlling substrate symmetry [26, 27]. In such single-crystalline materials with less defects, drastic κ reduction is difficult unless hetero-nanostructures are introduced. Actually, the introduction of ZnO layers into single-crystalline SnO_2 films with a thickness of ~240 nm reduced κ up to 3.2 $Wm^{-1}K^{-1}$ [28]. However, the $S^2\sigma$ of the single-crystalline SnO_2 films containing ZnO layers were half those of the films without hetero-nanostructures. Therefore, it is demanded to establish the methodology of drastically reducing κ while maintaining a high $S^2\sigma$ comparable to single-crystalline SnO_2 films.

In this study, we substantially reduce κ while maintaining a high $S^2\sigma$ by selectively manipulating the O^{2-} anion in domain-engineered SnO_2 with conduction and valence bands mainly composed of Sn5s and O2p orbitals, respectively (Figure 1). The ion implantation brought the selective O^{2-} anion manipulation, which has not been focused on in ever reported papers although some previous studies have attempted to control TE properties through ion implantation [29-31]. We expect that ion implantation can generate O defects (O vacancy introduction or anion displacement) more easily than Sn defects because lighter elements are more easily manipulated. The lattice thermal conductivity κ_{lat} of Arsenic (As)-implanted epitaxial SnO_2 films with manipulated O^{2-} anions (2.6 $Wm^{-1}K^{-1}$) was approximately half that of Sb-doped films without them (4.7 $Wm^{-1}K^{-1}$), while the maximum $S^2\sigma$ of As-implanted epitaxial SnO_2 films remained relatively high owing to the high S originating from the m^* increase. This O^{2-} anion manipulation is an outstanding methodology of selectively causing κ reduction while maintaining high $S^2\sigma$ in oxide TE materials.

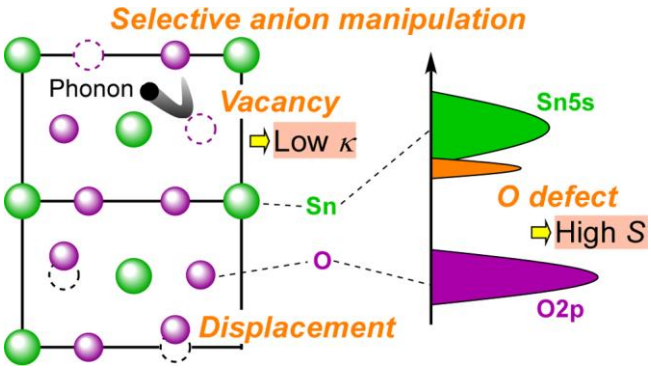

Figure 1. Schematic of TE property enhancement in an epitaxial SnO_2 film via selective O^{2-} anion manipulation. Selectively-manipulating O^{2-} anion (O vacancy introduction or anion displacement) forming valence band (O2p) can cause phonon scattering. Then, O defect resonant level increases m^*, leading to S enhancement.

METHOD

Epitaxial SnO_2 films/r-Al_2O_3 substrates were grown using pulsed laser deposition. As implantation was performed because of its lighter atomic mass and smaller radius than Sn, which brings large κ reduction. The epitaxial SnO_2 films were doped with As in the dose amount range of 2×10^{13}-2×10^{15} cm^{-2} using ion implantation. As a result, the epitaxial SnO_2 films were composed of doped (58 nm) and undoped layers. The sample information is described in Supporting Information 1. The thickness of the As-implanted sample was measured using cross-sectional scanning electron microscopy (SEM) with a 10 keV incident electron beam. The crystal structure was analyzed using X-ray diffraction (XRD) with a Cu K_α line (wavelength: 0.15406 nm). Then, the XRD peaks were assigned with the crystal information of SnO_2 (tetragonal and $P4_2/mnm$). The XRD pole figure measurement was conducted under the condition that the tilt angle ψ ranged from 0-75° and the rotation angle ϕ ranged from 0-360°. The analysis for defect formation was performed using Raman spectroscopy (laser wavelength: 532 nm) and X-ray photoelectron spectroscopy (XPS). Nanoscale structural observation was performed using high-resolution transmission electron microscopy (HRTEM) with a 200 keV electron beam in the incident direction of $<\bar{1}2\bar{1}0>_{Al_2O_3}$.

SEM observation, XRD pole figure measurement, Raman spectra measurement, XPS measurement, and HRTEM observation were conducted on the As-implanted sample with the dose amount of 1×10^{14} cm^{-2} as the representative sample. The σ, carrier concentration n, and S along the in-plane direction were obtained using the van der Pauw method, Hall effect measurement, and ZEM-3 (Advance Riko Inc.), respectively. The contribution of the undoped SnO_2 layer to electrical conduction was evaluated on the basis of the parallel conduction model, confirming that the contributions of the undoped SnO_2 layers were negligible. Therefore, we plotted the measured data, which we considered not to include the contributions of the undoped SnO_2 layers. The out-of-plane κ of the undoped and doped samples were measured using the time domain thermoreflectance (TDTR) and 2ω methods (Supporting information 2) [32, 33], respectively. For the As-implanted samples, the out-of-plane κ of the As-implanted layer was extracted via fitting analyses (Supporting information 2). In both κ measurements, Mo transducer films with a thickness of ~200 nm were deposited on the samples to detect TR signal. In 2ω method, the κ measurement was performed using the interfacial thermal resistances of Mo/SnO_2 film and SnO_2 film/r-Al_2O_3 measured by TDTR.

RESULTS AND DISCUSSION

Structural analysis

Figure 2a shows a photograph of the As-implanted sample. The characters of “Osaka Univ.” can be clearly observed. This indicates that the As-implanted sample has high optical transmittance, highlighting its high potential as a transparent TE material. The cross-sectional structures of SnO_2 films were observed using SEM (Figure 2b).The dark and bright regions are considered to correspond to Al_2O_3 substrates and SnO_2 films, respectively. This reveals the growth of SnO_2 films with the thickness of ~120-150 nm.

XRD measurement was performed to analyze the crystal structures of the samples. Figure 2c shows the XRD 2θ-ω scans of an undoped sample and three conventional As-implanted samples with different dose amount (1×10^{14}, 8×10^{14}, and 2×10^{15} cm^{-2}). In all the samples, the XRD peaks coming from $(101)_{SnO_2}$, $(\bar{1}012)_{Al_2O_3}$ and $(\bar{2}024)_{Al_2O_3}$ appeared at the 2θ of ~33.9º, ~25.6º and ~52.5º, respectively. No shift of the XRD peaks coming from $(101)_{SnO_2}$ was observed in any samples, indicating no lattice constant change. Thus, it was found that the crystal structures of the samples were maintained even after As implantation. To confirm the epitaxial growth of the As-implanted samples, we obtained an XRD pole figure at the fixed 2θ of ~26.6º, corresponding to $\{110\}_{SnO_2}$, as shown in Figure 2d. The XRD pole figure revealed that there were two peaks at the ψ of ~70º although there should be four peaks in the case of epitaxial SnO_2 films/r-Al_2O_3 substrates, which correspond to two epitaxial relationships: the relationship of $(101)_{SnO_2}//(\bar{1}012)_{Al_2O_3}$ with $[010]_{SnO_2}//[\bar{1}2\bar{1}0]_{Al_2O_3}$ and that rotated by 180º with respect to the $[\bar{1}012]_{Al_2O_3}$ axis. This is explained by the tilted growth, as reported in the previous studies [34, 35]. Anyway, it was found that SnO_2 films were epitaxially grown on r-Al_2O_3 substrates. The Sb-doped samples formed using the Sb-doped SnO_2 target in our previous study [26] also had no lattice change and the same epitaxial relationship as the As-implanted samples.

Raman spectroscopy measurements were performed to analyze defect formation in the samples. Figure 2e shows the Raman spectra of the undoped, As-implanted, and Sb-doped samples. The Raman spectra of all the samples displayed peaks around 574 cm^{-1} (A_1 mode [36]) although the intensity of the peak in the As-implanted samples was low owing to the surface damage coming from ion implantation. Through Gaussian fitting analyses, it was found that the peak of the As-implanted sample (~584 cm^{-1}) was slightly blue-shifted compared with those of the undoped (~582 cm^{-1}) and Sb-doped samples (~582 cm^{-1}). The previous study reported that the blue-shift of the A_1 mode could be attributed to the reduction of SnO_2 [36]. Therefore, the composition of the As-implanted samples likely differed from those of the other samples. For As-implanted sample, a significant additional peak appeared around 650 cm^{-1}. In a

previous theoretical study, the peak around 650 cm^{-1} appeared in SnO_2 crystals with O vacancy [37]. Therefore, the observed peak around 650 cm^{-1} in the As-implanted sample is likely attributed to O vacancy. On the other hand, the As-implanted sample did not exhibit a peak coming from the Sn vacancy around 670 cm^{-1} unlike the previous theoretical study on SnO_2 crystals with Sn vacancy [37]. The results indicate that the As-implanted samples had a larger number of O vacancies than the other samples, which is consistent with the XPS results (Supporting Information 3), and the As-implanted samples did not have Sn vacancies. That is, the As-implanted samples had selectively-manipulated O^{2-} anions. The fact that these O^{2-} anions did not alter the Sn state was revealed by XPS measurement (Supporting Information 3).

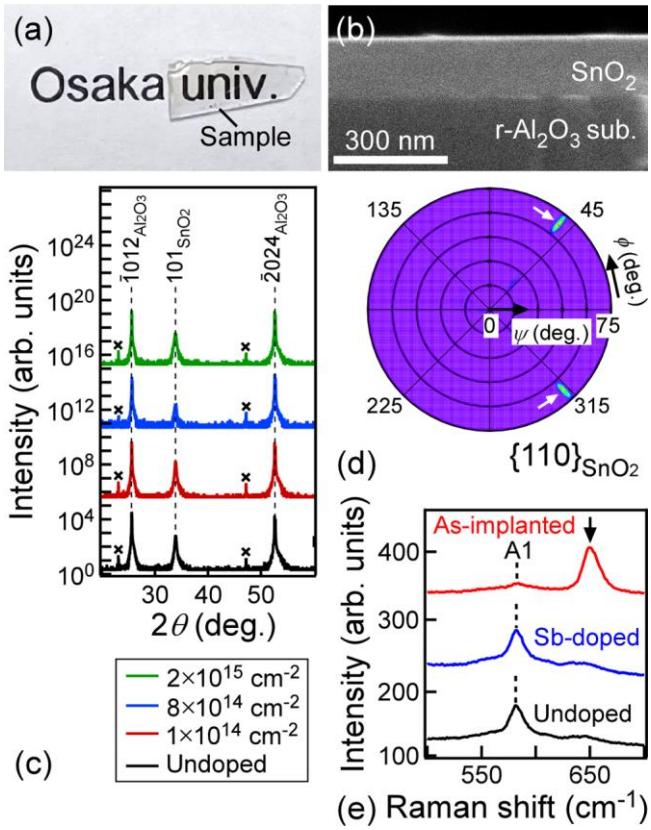

Figure 2 (a) Photograph of the As-implanted sample. (b) Cross-sectional SEM image of the As-implanted sample. (c) XRD 2θ-ω scans of the undoped and As-implanted samples with the dose amount of 1×10^{14}, 8×10^{14}, and 2×10^{15} cm^{-2}. The peaks at the 2θ of ~33.9º, ~25.6º and ~52.5º come from $(101)_{SnO_2}$, $(\bar{1}012)_{Al_2O_3}$ and $(\bar{2}024)_{Al_2O_3}$, respectively. The peaks originating from Cu K_β are denoted by the cross marks. (d) XRD pole figure of the As-implanted sample with the dose amount of 1×10^{14} cm^{-2}. (e) Raman spectra of the undoped, Sb-doped, and As-implanted (dose amount of 1×10^{14} cm^{-2}) samples. The broken lines and the solid arrow denote the positions of the peaks originating from the A_1 mode and O vacancy, respectively.

The nanoscale structures of the As-implanted samples were observed using cross-sectional HRTEM. Figure 3a shows a low-magnification TEM image. The SnO_2 films had a number of stacking

faults with the average spacing of ~22 nm. In other words, the SnO_2 film was composed of a crystal domain structure with an average size of ~22 nm. The crystal structures were identified by fast Fourier transform (FFT) analyses. Figures 3c and d are the FFT patterns of regions A and B in the high-magnification HRTEM image (Figure 3b), respectively. The FFT patterns of the regions A and B corresponded to the theoretical ones of Al_2O_3 and SnO_2, respectively. This reveals that the SnO_2 film was grown on r-Al_2O_3 substrate with the epitaxial relationship of $(101)_{SnO_2}//(\bar{1}012)_{Al_2O_3}$ with $[010]_{SnO_2}//[1\bar{2}10]_{Al_2O_3}$ out of the aforementioned two epitaxial relationships. The XRD and atomic force microscopy results of the Sb-doped SnO_2 film (crystal domain size: ~20 nm)/r-Al_2O_3 substrate [26] indicate that apart from O^{2-} anion manipulation, the As-implanted sample had the same structural features as the Sb-doped samples in terms of lattice constant, growth orientation, and crystal domain size. Therefore, the difference in TE properties of both samples can be attributed to the O^{2-} anion manipulation.

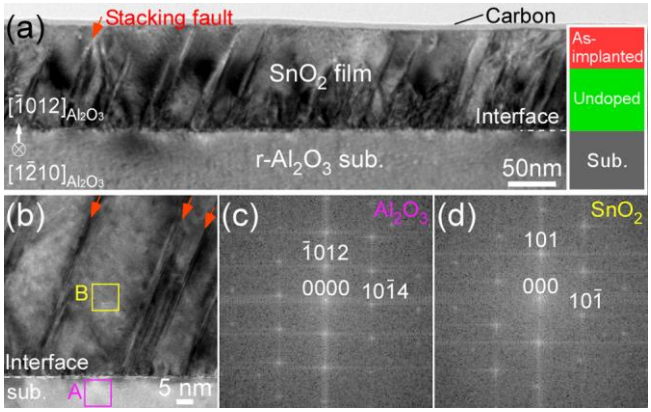

Figure 3 (a, b) Low-magnification TEM (a) and high-magnification HRTEM images (b). Inset of (a) shows the schematic of the As-implanted SnO_2 layer/undoped SnO_2 layer/r-Al_2O_3 substrate). In (a) and (b), the solid arrows denote the stacking faults. (c, d) FFT patterns of the solid square regions A (c) and B (d) in (b).

Thermoelectric properties

Figures 4a-d show the μ, σ, S, and $S^2\sigma$ of the As-implanted samples at room temperature, respectively. For comparison, we simultaneously plotted the data of the Sb-doped samples in Figures 4a-d and the semi-empirical curve of SnO_2 bulk in Figures 4a and b [26, 38]. The μ of the As-implanted samples decreased as n increased (Figure 4a). This tendency can be explained by ionized impurity scattering. The As-implanted samples exhibited lower μ than the Sb-doped samples and SnO_2 bulk at the same n. Owing to the lower μ, the σ of the As-implanted samples were lower than those of the other samples at the same n (Figure 4b). On the other hand, the As-implanted samples exhibited higher S than the Sb-doped samples at the same n (Figure 4c). The higher S and lower μ of the As-implanted samples can be brought by an m^* increase originating from the formation of the O vacancy level, which is reportedly close to the conduction band minimum [39]. The $S^2\sigma$ of the sample with the dose amount of 1×10^{14} cm^{-2} reached ~3.0 $\mu Wcm^{-1}K^{-2}$ at the n of ~3×10^{19} cm^{-3} (Figure 4d). Because S of As-implanted samples increased despite the decrease in σ, $S^2\sigma$ remained relatively high: 3/4 of the maximum $S^2\sigma$ of the Sb-doped samples (~4.0 $\mu Wcm^{-1}K^{-2}$). This relatively high $S^2\sigma$ in the As-implanted samples was also achieved at high T (Supporting Information 4). If the κ of the As-implanted samples was less than 3/4 of the κ of the Sb-doped samples, the TE property of the As-implanted samples could exceed that of the Sb-doped samples.

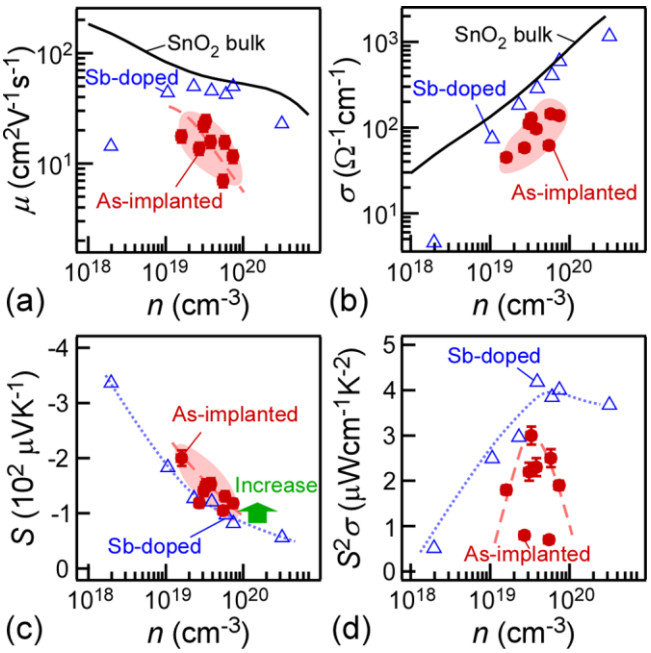

Figure 4 (a-d) μ (a), σ (b), S (c), and $S^2\sigma$ (d) of the As-implanted samples as a function of n at room temperature, where experimental data of the Sb-doped samples are simultaneously plotted [26]. In (a-d), the solid circles and the open triangles are the experimental data of the As-implanted and Sb-doped samples, respectively. The solid curves in (a) and (b) are semi-empirical curves of the SnO_2 bulk. The broken curves in (a), (c) and (d) are eye-guides for As-implanted samples. The dotted curves in (c) and (d) are eye-guides for Sb-doped samples.

Figure 5a summarizes the out-of-plane κ of the As-implanted sample with the dose amount of 1×10^{14} cm^{-2} and the Sb-doped sample [26] at room temperature. For comparison, the κ of the undoped SnO_2 bulk is also shown in Figure 5a [40]. The κ of the As-implanted sample (~2.7 $Wm^{-1}K^{-1}$) was the smallest among them. This value was ~1/20 (~1/2) of those of the undoped SnO_2 bulk (the Sb-doped sample). Considering this substantial κ reduction and the aforementioned suppression of $S^2\sigma$ decrease, it was found that the As-implanted samples have higher TE property than the Sb-doped samples. To evaluate the contribution of κ_{lat}, we removed the electron contribution to κ using the Lorenz number which was calculated by using the Boltzmann transport equation (Supporting Information 5). Figure 5b summarizes

the out-of-plane κ_{lat} of the As-implanted and the Sb-doped samples, and the κ_{lat} of undoped SnO_2 bulk. The As-implanted samples exhibited a smaller κ_{lat} (2.6 $Wm^{-1}K^{-1}$) than the Sb-doped samples (4.7 $Wm^{-1}K^{-1}$ [26]) and undoped SnO_2 bulk (55 $Wm^{-1}K^{-1}$ [40]). A remarkable fact is that As implantation substantially reduced κ_{lat}.

Let us discuss the physical mechanism of the κ_{lat} difference between the As-implanted and Sb-doped samples. First, there is no κ_{lat} difference brought by the anisotropy of the phonon group velocity or the density of the domain interface because the As-implanted samples had the same lattice constant, epitaxial relationship, and domain size as the Sb-doped samples. Therefore, three possible hypotheses can be considered for the κ_{lat} difference: 1. Difference in dopant amount; 2. Film thickness effect; 3. As implantation effect. For the Sb-doped sample with a κ_{lat} of ~4.7 $Wm^{-1}K^{-1}$, the dopant amount was 0.2 at% (5.6×10^{19} cm^{-3}). On the other hand, the dose amount of As-implanted sample (1×10^{14} cm^{-2}) simply corresponded to the dopant amount per unit volume of ~2.4×10^{19} cm^{-3} (Supporting information 1). These indicate that the As-implanted sample has a smaller number of dopants than the Sb-doped sample. This rules out hypothesis 1.

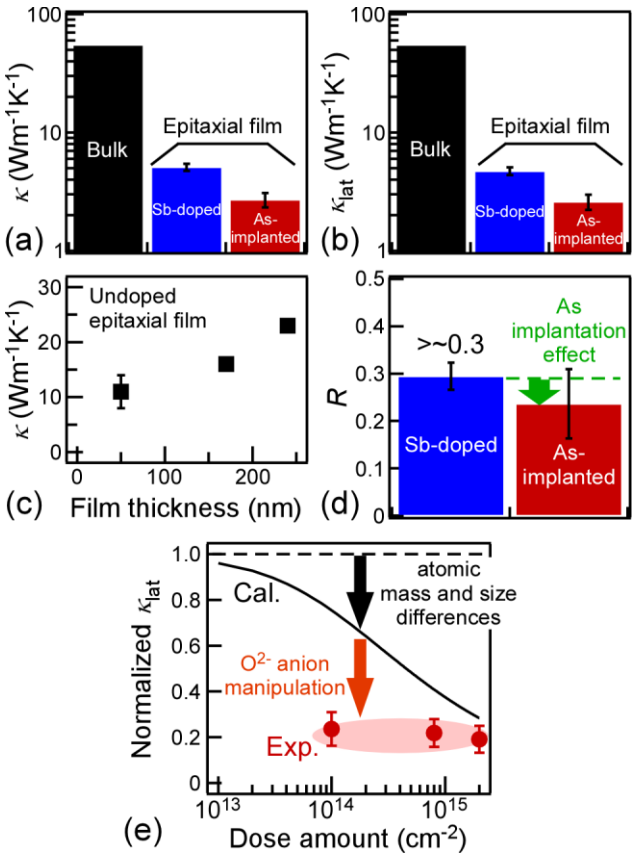

Figure 5 (a, b) Out-of-plane κ (a) and κ_{lat} (b) of the undoped SnO_2 bulk [40], Sb-doped sample, and As-implanted sample at room temperature. (c) Film thickness dependence of κ for undoped epitaxial SnO_2 films/r-Al_2O_3. (d) R values of the As-implanted and Sb-doped samples. (e) Normalized κ_{lat} of As-implanted sample as a function of dose amount. The solid circles are the experimental data of As-implanted samples. The solid curve is the calculation using Debye-Callaway model with impurity and Umklapp scatterings.

It is required to consider the hypothesis 2 because the thickness of the As-implanted sample (58 nm) differs from that of the Sb-doped sample (120 nm). To verify the film thickness effect on κ_{lat}, we measured the κ ($\sim\kappa_{lat}$) of various undoped epitaxial SnO_2 films with different thicknesses (50, 170, and 240 nm), as shown in Figure 5c. The κ of the undoped epitaxial SnO_2 films increased with increasing film thickness, indicating that SnO_2 films have the film thickness dependence of κ within the thickness range

of 50-240 nm. We calculated the rate R of the κ_{lat} of the doped samples to those of undoped SnO_2 films with almost the same thicknesses to approximately remove the film thickness effect on κ_{lat}. Therein, we used the κ_{lat} of the As-implanted sample (Sb-doped sample) with a thickness of 58 nm (120 nm) and κ_{lat} of the undoped sample with a thickness of 50 nm (170 nm). The R value of the As-implanted sample with the dose amount of 1×10^{14} cm^{-2} (~0.23) was smaller than that of the Sb-doped sample (~0.3) (Figure 5d). In the case of Sb-doped sample, R should be larger than 0.3 because the κ_{lat} of the undoped sample with a thickness exceeding 120 nm was used. These indicate that the κ_{lat} reduction of As-implanted sample is brought not only by the hypothesis 2 but also by the hypothesis 3.

The effect of As implantation on κ_{lat} includes two contributions: larger atomic mass and greater size differences between As and Sn than that between Sb and Sn; O^{2-} anion manipulation. From a theoretical viewpoint of the impurity phonon scattering process, larger atomic mass and greater size differences clearly contribute to κ_{lat} reduction. Therefore, we discuss whether O^{2-} anion manipulation contributes to κ_{lat} reduction or not. To clarify this contribution, we measured the experimental normalized κ_{lat} as a function of dose amount (Figure 5e), where normalized κ_{lat} is defined as the κ_{lat} of the As-implanted samples divided by the κ_{lat} of the undoped sample with a thickness of 50 nm. The experimental normalized κ_{lat} was compared with the theoretical κ_{lat} calculated using Debye-Callaway model with impurity and Umklapp scatterings [41-45] (Supporting Information 6), which does not include O^{2-} anion manipulation and lattice change contributions. The experimental normalized κ_{lat} values were lower than the theoretical values at the same dose amount. Because the theoretical normalized κ_{lat} includes no contribution of O^{2-} anion manipulation (Figure 5e), it is considered that lower experimental normalized κ_{lat} than the theoretical one was brought by O^{2-} anion manipulation. This indicates that not only As introduction but also O^{2-} anion manipulation contributes to κ_{lat} reduction.

CONCLUSIONS

This study demonstrated that O^{2-} anion manipulation through ion implantation to epitaxial SnO_2 films is a promising approach for reducing κ while maintaining a high $S^2\sigma$. Implanting As into undoped epitaxial SnO_2 films/r-Al_2O_3 substrates selectively generated O vacancies. The κ_{lat} of the As-implanted samples (2.6 $Wm^{-1}K^{-1}$) was approximately half that of the Sb-doped samples (4.7 $Wm^{-1}K^{-1}$), whereas the maximum $S^2\sigma$ of the As-implanted epitaxial SnO_2 films with manipulated O^{2-} anions remained relatively high owing to the high S originating from an m^* increase. Interestingly, the experimental κ_{lat} of the As-implanted samples were lower than the theoretical ones which were calculated by solely introducing the contributions of As impurity and Umklapp scattering processes under the condition that no lattice constant is changed and no O^{2-} anion is manipulated, indicating that not only As introduction but also O^{2-} anion manipulation contributed to κ_{lat} reduction. This O^{2-} anion manipulation will contribute to the development of oxide TE material as an outstanding methodology of selectively causing κ reduction while maintaining high $S^2\sigma$.

ASSOCIATED CONTENT

Supporting Information.

The Supporting Information is available free of charge on the ACS Publication website at DOI: Sample information, Thermal conductivity measurement for As-implanted samples, X-ray photoelectron spectroscopy analysis, Temperature dependences of thermoelectric properties, Calculation of Lorenz number, and Detail of lattice thermal conductivity calculation.

AUTHOR INFORMATION

Corresponding Author

E-mail: nakamura.yoshiaki.es@osaka-u.ac.jp

Author Contributions

Y. K. and S. K. prepared film samples. S. K., Y. K., Y. U., and T. Y. characterized the samples. T. I. analyzed the measurement data. Y. Y. measured κ of the samples. N. N. and Y. M. carried out TEM observations. E. K. performed XPS measurement. T. I. and Y. N. discussed and wrote the paper. Y. N. is the principal investigator. All authors discussed the results and contributed to the final manuscript.

Notes

The authors declare no competing financial interest.

ACKNOWLEDGEMENTS

This study was supported by a Grant-in-Aid for Scientific Research A (No. 23H00258), for Scientific Research B (No. 23H01361), and for Early-Carrier Scientists (No. 24K17613). A part of this study was supported by "ARIM Project of the Ministry of Education, Culture, Sports, Science and Technology, Japan (MEXT), Grant No. JPMXP1224OS0007" at the Research Center for Ultra High Voltage Electron Microscopy (Nanotechnology Open Facilities) in Osaka University.

REFERENCES

[1] Kleinke, H. New Bulk Materials for Thermoelectric Power Generation: Clathrates and Complex Antimonides. *Chem. Mater.* **2010**, 22, 604-611.

[2] Williams, D. E.; Rietman, J. A.; Maier, J. M.; Tan, R.; Greytak, A. B.; Smith, M. D.; Krause, J. A.; Shustova, N. B. Energy Transfer on Demand: Photoswitch-Directed Behavior of Metal−Porphyrin Frameworks. *J. Am. Chem. Soc.* **2014**, 136, 11886-11889.

[3] Huh, W.; Lee, D.; Lee, C. –H. Memristors Based on 2D Materials as an Artificial Synapse for Neuromorphic Electronics. *Adv. Mater.* **2020**, 32, 2002092.

[4] Zebarjadi, M.; Joshi, G.; Zhu, G.; Yu, B.; Minnich, A.; Lan, Y.; Wang, X.; Dresselhaus, M.; Ren, Z.; Chen, G. Power Factor Enhancement by Modulation Doping in Bulk Nanocomposites. *Nano Lett.* **2011**, 11, 2225-2230.

[5] Neophytou, N.; Kosina, H. Optimizing Thermoelectric Power Factor by Means of A Potential Barrier. *J. Appl. Phys.* **2013**, 114, 044315.

[6] Nakamura, Y.; Isogawa, M.; Ueda, T.; Yamasaka, S.; Matsui, H.; Kikkawa, J.; Ikeuchi, S.; Oyake, T.; Hori, T.; Shiomi, J.; Sakai, A. Anomalous Reduction of Thermal Conductivity in Coherent Nanocrystal Architecture for Silicon Thermoelectric Material. *Nano Energy* **2015**, 12, 845-851.

[7] Nakamura, Y. Nanostructure Design for Drastic Reduction of Thermal Conductivity while Preserving High Electrical Conductivity. *Sci. Technol. Adv. Mater.* **2018**, 19, 31-43.

[8] Ishibe, T.; Tomeda, A.; Watanabe, K.; Kamakura, Y.; Mori, N.; Naruse, N.; Mera, Y.; Yamashita, Y.; Nakamura, Y. Methodology of Thermoelectric Power Factor Enhancement by Controlling Nanowire Interface. *ACS Appl. Mater. Interfaces* **2018**, 10, 37709-33716.

[9] Zhang, Q.; Song, Q.; Wang, X.; Sun, J.; Zhu, Q.; Dahal, K.; Lin, X.; Cao, F.; Zhou, J.; Chen, S.; Chen, G.; Mao, J.; Ren, Z. Deep Defect Level Engineering: a Strategy of Optimizing the Carrier Concentration for High Thermoelectric Performance. *Energy Environ. Sci.* **2018**, 11, 933-940.

[10] Narducci, D. Thermoelectric Harvesters and the Internet of Things: Technological and Economic Drivers. *J. Phys. Energy* **2019**, 1, 024001.

[11] Ming, H.; Zhu, G.; Zhu, C.; Qin, X.; Chen, T.; Zhang, J.; Li, D.; Xin, H.; Jabar, B. Boosting Thermoelectric Performance of Cu_2SnSe_3 via Comprehensive Band Structure Regulation and Intensified Phonon Scattering by Multidimensional Defects. *ACS Nano* **2021**, 15, 10532-10541.

[12] Cao, Y.; Bai, H.; Li, Z,; Zhang, Z.; Tang, Y.; Su, X.; Wu, J.; Tang, X. Zn-Induced Defect Complexity for the High Thermoelectric Performance of n-Type PbTe Compounds. *ACS Appl. Mater. Interfaces* **2021**, 13, 43134-43143.

[13] Su, L.; Wang, D.; Wang, S.; Qin, B.; Wang, Y.; Qin, Y.; Jin, Y.; Chang, C.; Zhao, L. D. High Thermoelectric Performance Realized through Manipulating Layered Phonon-Electron Decoupling. *Science* **2022**, 375, 1385-1389.

[14] Terada, T.; Uematsu, Y.; Ishibe, T.; Naruse, N.; Sato, K.; Nguyen, T. Q.; Kobayashi, E.; Nakano, H.; Nakamura, Y. Giant Enhancement of Seebeck Coefficient by Deformation of Silicene Buckled Structure in Calcium-Intercalated Layered Silicene Film. *Adv. Mater. Interfaces* **2022**, 9, 2101752.

[15] Abbas, A.; Nisar, M.; Zheng, Z, H,; Li, F.; Jabar, B.; Liang, G.; Fan, P.; Chen, Y. X. Achieving High Thermoelectric Performance of Eco-Friendly SnTe-Based Materials by Selective Alloying and Defect Modulation. *ACS Appl. Mater. Interfaces* **2022**, 14, 25802-25811.

[16] Wang, D. Z.; Liu, W. D.; Mao, Y.; Li, S.; Yin, L. C.; Wu, H.; Li, M.; Wang, Y.; Shi, X. L.; Yang, X.; Liu, Q.; Chen, Z. G. Decoupling Carrier-Phonon Scattering Boosts the Thermoelectric Performance of n-Type GeTe-Based Materials. *J. Am. Chem. Soc.* **2024**, 146, 1681-1689.

[17] Hu, L.; Zhu, T.; Liu, X.; Zhao, X. Point Defect Engineering of High-Performance Bismuth-Telluride-Based Thermoelectric Materials. *Adv. Funct. Mater.* **2014**, 24, 5211-5218.

[18] Xie, L.; Chen, Y.; Liu, R.; Song, E.; Xing, T.; Deng, T.; Song, Q.; Liu, J.; Zheng, R.; Gao, X.; Bai, S.; Chen, L. Stacking Faults Modulation for Scattering Optimization in GeTe-Based Thermoelectric Materials. *Nano Energy* **2020**, 68, 104347.

[19] Karthikeyan, V.; Oo, S. L.; Surjadi, J. U.; Li, X. C.; Theja, V.C.S.; Kannan, V.; Lau, S. C.; Lu, Y.; Lam, K. H.; Roy, V. A. L. Defect Engineering Boosted Ultrahigh Thermoelectric Power Conversion Efficiency in Polycrystalline SnSe. *ACS Appl. Mater. Interfaces.* **2021**,13, 58701-58711.

[20] Jiang, Y.; Dong, J.; Zhuang, H.-L.; Yu, J.; Su, B.; Li, H.; Pei, J.;Sun, F.-H.; Zhou, M.; Hu, H.; Li, J.-W.; Han, Z.; Zhang, B.-P.; Mori,T.; Li, J.-F. Evolution of Defect Structures Leading to High ZT in GeTe-Based Thermoelectric Materials. *Nat. Commun.* **2022**, 13, 6087.

[21] Thébaus, S.; Adessi, Ch.; Bouzerar, G. Large Enhancement of the Thermoelectric Power Factor in Disordered Materials through Resonant Scattering. *Phys. Rev. B* **2019**, 99, 245203.

[22] Parashchuk, T.; Wiendlocha, B.; Cherniushok, O.; Knura, R.; Wojciechowski, K. T. High Thermoelectric Performance of P-type PbTe Enabled by the Synergy of Resonance Scattering and Lattice Softening. *ACS Appl. Mater. Interfaces* **2021**, 13, 49027-49042.

[23] Heremans, J. P.; Wiendlocha, B.; Chamoire, A. M. Resonant Levels in Bulk Thermoelectric Semiconductors. *Energy Environ. Sci.* **2012**, 5, 5510-5530.

[24] Wang, H.; Cao, X.; Takagiwa Y.; Snyder, G. J. Higher Mobility in Bulk Semiconductors by Separating the Dopants from the Charge Conducting Band – a Case Study of Thermoelectric PbSe. *Mater. Horiz.* **2015**, 2, 323-329.

[25] Zeier, W. G.; Zevalkink, A.; Gibbs, Z. M.; Hautier, G.; Kanatzidis, M. G.; Snyder, G. J. Thinking like a Chemist: Intuition in Thermoelectric Materials. *Angew. Chem. Int. Ed.* **2016**, 55, 6826-6841.

[26] Ishibe, T.; Tomeda, A.; Komatsubara, Y.; Kitaura, R.; Uenuma, M.; Uraoka, Y.; Yamashita, Y.; Nakamura, Y. Carrier and Phonon Transport Control by Domain Engineering for High-Performance Transparent Thin Film Thermoelectric Generator. *Appl. Phys. Lett.* **2021**, 118, 151601.

[27] Ishibe, T.; Komatsubara, Y.; Ishikawa, K.; Takigawa, S.; Naruse, N.; Mera, Y.; Yamashita, Y.; Ohishi, Y.; Nakamura, Y. Boosting Thermoelectric Performance in Epitaxial GeTe Film/Si by Domain Engineering and Point Defect Control. *ACS Appl. Mater. Interfaces* **2023**, 15, 26104-26110.

[28] Ishibe, T.; Komatsubara, Y.; Katayama, T.; Yamashita, Y.; Naruse, N.; Mera, Y.; Hattori, A. N.; Tanaka, H.; Nakamura, Y. Interface Design of Transparent Thermoelectric Epitaxial ZnO/SnO_2 Multilayer Film for Simultaneous Realization of Low Thermal Conductivity and High Optical Transmittance. *Appl. Phys. Lett.* **2023**, 122, 041603.

[29] Hughes, M. A.; Fedorenko, Y.; Gholipour, B.; Yao, J.; Lee, T. –H.; Gwilliam, R. M.; Homewood, K. P.; Hinder, S.; Hewak, D. W.; Elliott, S. R.; Curry, R. J. N-Type Chalcogenide by Ion Implantation. *Nat. Commun.* **2014**, 5, 5346.

[30] Tureson, N.; Marteau, M.; Cabioch, T.; Nong, N. V.; Jensen, J.; Lu, J.; Greczynski, G.; Fournier, D.; Singh, N.; Soni, A.; Belliard, L.; Eklund, P.; Febvrier, A. L. Effect of Ion-Implantation-Induced Defects and Mg Dopants on the Thermoelectric Properties of ScN. *Phys. Rev. B* **2018**, 98, 205307.

[31] Burcea, R.; Barbot, J. –F.; Renault, P. –O.; Eyidi, D.; Girardeau, T.; Marteau, M.; Giovannelli, F.; Zenji, A.; Rampnoux, J. –M.; Dilhaire, S.; Eklund, P.; Febvrier, A. L. Influence of Generated Defects by Ar Implantation on the Thermoelectric Properties of ScN. *ACS Appl. Energy Mater.* **2022**, 5, 11025-11033.

[32] Ishibe, T.; Okuhata, R.; Kaneko, T.; Yoshiya, M.; Nakashima, S.; Ishida, A.; Nakamura, Y. Heat Transport through Propagon-Phonon Interaction in Epitaxial Amorphous-Crystalline Multilayers. *Commun. Phys.* **2021**, 4, 153.

[33] Ishibe, T.; Kaneko, T.; Uematsu. Y.; Akaba H. S-.; Komura, M.; Iyoda, T.; Nakamura, Y. Tunable Thermal Switch via Order-Order Transition in Liquid Crystalline Block Copolymer. *Nano Lett.* **2022**, 22, 6105-6111.

[34] Choudhary, R. J.; Ogale, S. B.; Kulkarni, V. N.; Venkatesan, T.; Harshavardhan, K. S.; Strikovski, M.; Hannoyer, B. Pulsed-Electron-Beam Deposition of Transparent Conducting SnO_2 Films and Study of Their Properties. *Appl. Phys. Lett.* **2004**, 84, 1483-1485.

[35] Lahiji, F. A. F.; Paul, B.; Febvrier, A. L.; Eklund, P. Unusual Tilted Growth and Epitaxial Relationship of NaCl B1-Structured NiO and CrN on R-plane Al_2O_3. *J. Appl. Phys.* **2004**, 135, 065302.

[36] Shek, C. H.; Lin, G. M.; Lai, J. K. L. Effect of Oxygen Deficiency on the Raman Spectra and Hyperfine Interactions of Nanometer SnO_2. *Nanostruct. Mater.* **1999**, 11, 831−835.

[37] Kraus, M.; Hoppe, M.; Muñiz, C. R.; Mendez, A.; Munnik, F.; Valenzuela, A. G.; Schimp, C.; Rafaja D.; Galindo, R. E. Exceptionally High-Temperature in-air Stability of Transparent Conductive Oxide Tantalum-Doped Tin Dioxide. *J. Mater. Chem. A* **2023**, 11, 17686-17698.

[38] Ellmer, K.; Mientus, R. Carrier Transport in Polycrystalline Transparent Conductive Oxides: A Comprehensive Study of Zinc Oxide and Indium Oxide. *Thin Solid Films* **2008**, 516, 4620-4627.

[39] Samson, S.; Fonstad, C. G. Defect Structure and Electronic Donor Levels in Stannic Oxide Crystals. *J. Appl. Phys.* **1973**, 44, 4618-4621.

[40] Türkes, P.; Pluntke, Ch.; Helbig, R. Thermal Conductivity of SnO_2 Single Crystals. *J. Phys. C: Solid St. Phys.* **1980**, 13, 4941-4951.

[41] He. J.; Girard, S. N.; Kanatzidis, M. G.; Dravid, V. P. Microstructure-Lattice Thermal Conductivity Correlation in Nanostructured $PbTe_{0.7}S_{0.3}$ Thermoelectric Materials. *Adv. Funct. Mater.* **2010**, 20, 764-772.

[42] Wang, Z.; Alaniz, J. E.; Jang, W.; Garay, J. E.; Dames, C. Thermal Conductivity of Nanocrystalline Silicon: Importance of Grain Size and Frequency-Dependent Mean Free Paths. *Nano Lett.* **2011**, 11, 2206-2213.

[43] Zhao, L.; Wu, J. J.; Hao, S. Q.; Wu, C. I.; Zhou, X. Y.; Biswas, K.; He, J. Q.; Hogan, T. P.; Uher, C.; Wolverton, C.; Dravid, V. P.; Kanatzidis, M. G. All-Scale Hierarchical Thermoelectrics: MgTe in PbTe Facilitates Valence Band Convergence and Suppresses Bipolar Thermal Transport for High Performance. *Energy Environ. Sci.* **2013**, 6, 3346-3355.

[44] Yang, J.; Meisner, G. P.; Chen, L. Strain Field Fluctuation Effects on Lattice Thermal Conductivity of ZrNiSn-Based Thermoelectric Compounds. *Appl. Phys. Lett.* **2004**, 85, 1140-1142.

[45] Li, J.; Xie, Y.; Zhang, C.; Ma, K.; Liu, F.; Ao, W.; Li, Y.; Zhang, C. Stacking Fault-Induced Minimized Lattice Thermal Conductivity in the High-Performance GeTe-Based Thermoelectric Materials upon Bi_2Te_3 Alloying. *ACS Appl. Mater. Interfaces* **2019**, 11, 20064-20072.

Table of Contents